

## SPHERE-3 Project for Studying the Composition of Primary Cosmic Rays in the Energy Range Between 1 and 1000 PeV

D. V. Chernov<sup>1)\*</sup>, C Azra<sup>2)</sup>, E. A. Bonvech<sup>1)</sup>, V. I. Galkin<sup>1),2)</sup>, V. A. Ivanov<sup>2)</sup>,  
V. S. Latypova<sup>2)</sup>, D. A. Podgrudkov<sup>1),2)</sup>, and T. M. Roganova<sup>1)</sup>

Received July 19, 2022; revised July 19, 2022; accepted July 21, 2022

**Abstract**—A determination of the composition of primary cosmic rays in the energy range between 1 and 1000 PeV is an important objective in studies of processes involving the formation and propagation of cosmic rays. On the basis of experience gained in exploiting the SPHERE-2 balloon-based facility, a SPHERE-3 facility, which possesses a wider aperture and a better optical resolution, is developed. The current status of work on designing this facility is presented.

**DOI:** 10.1134/S1063778822060059

### 1. INTRODUCTION

In recent years, there appeared pieces of evidence that a significant part of nuclei of primary cosmic rays (PCR) with energies in the range between 1 and 1000 PeV may have an extragalactic origin [1]. Investigation of PCR composition at these energies may be of crucial importance in choosing a model for the transition from galactic to extragalactic cosmic rays. This in turn is of importance for developing a global picture of acceleration and propagation of cosmic rays. At the present time, the problem of PCR mass composition at ultrahigh energies above 1 PeV is far from being solved conclusively [2–4]. The KASCADE-Grande Collaboration was able to single out the spectra of two groups of nuclei [5], but uncertainties in the strong-interaction model hindered a more detailed classification. Despite several decades of studies devoted to measuring the PCR composition by indirect methods on the basis of components of extensive air showers (EAS) and tens of experiments already performed, partial spectra of groups of nuclei have not been measured at energies above 1 PeV. Moreover, the results of different experiments on the average logarithm of the mass number in the energy range between 3 and 50 PeV differ severalfold [4–8]. The attempt at creating a global model of partial spectra over a wide range of primary energies in [9] runs into the absence of a published estimate of systematic errors in the studies of some experimental

groups and suffers from the uncertainties in nuclear-interaction models; therefore, it may only furnish impetus to continuing investigations. Meanwhile, good knowledge of the spectra of groups of nuclei is necessary for testing various models of PCR acceleration and propagation. Therefore, the implementation of new experiments that would be sensitive to the nuclear composition of cosmic rays is a task of importance for modern astrophysics.

### 2. METHOD OF REFLECTED CHERENKOV LIGHT

The SPHERE project is aimed at solving the problem of determining PCR nuclear composition by the method proposed by Academician A.E. Chudakov [10] and based on the detection of EAS optical Cherenkov radiation (more frequently called Cherenkov light) reflected from the snow surface of earth.

This method provides a significant area of detection of Cherenkov light by means of a compact instrument lifted above the snow surface. The Cherenkov EAS component is assumed to be the least dependent on the interaction model; therefore, the method based on its detection is expected to give the most accurate estimate of the PCR energy. Also, a change in the detector altitude permits measuring the same range of PCR energies with different resolutions since the distance between the centers of the fields of view of neighboring sensitive elements changes. This in turn makes it possible to control systematic errors that may arise in developing a procedure for reconstructing primary features of PCR. The field of view of each sensitive element (pixel) of the detector covers a significant part of the surveyed area. With

<sup>1)</sup>Skobeltsyn Institute of Nuclear Physics, Moscow State University, Moscow, Russia.

<sup>2)</sup>Faculty of Physics, Moscow State University, Moscow, Russia.

\*E-mail: chr@dec1.sinp.msu.ru

allowance for a partial overlap of the fields of view of neighboring pixels, this makes it possible to observe EAS Cherenkov light near the shower axis in the majority of events. Usually, this is beyond the scope of possibilities of widely spaced ground-based detectors. This circumstance improves substantially accuracy in assessing the type of primary particles since the intensity of Cherenkov light in the near-axis region is sensitive to variations of the EAS cascade from various types of PCR nuclei [11, 12].

A high sensitivity in estimating the chemical composition of PCR relies on an analysis of each individual distribution of EAS Cherenkov light. The application of both one-parameter and multiparameter mass criteria [13] makes it possible to estimate the primary-particle mass in an individual event and not through an analysis of a parameter averaged over a large number of “typical” events (for example,  $X_{\max}$ ). A good methodological purity both in determining the energy of PCR particles and in estimating the chemical composition is reached owing to the absence of interplay of the algorithms of these procedures.

This method of detection of reflected EAS Cherenkov light was successfully implemented in the balloon-borne experiment with the SPHERE-2 facility in the period spanning the years 2008 and 2013 [13–19]. The SPHERE-2 facility [15] was created at Institute of Nuclear Physics, Moscow State University, with the support of Lebedev Physical Institute and Institute for Nuclear Research, Russian Academy of Sciences. The facility is based on a spherical mirror 1.5 m in diameter and involving a mosaic formed by 109 photomultiplier tubes PMT-84-3 at the focus of the mirror. It also includes 109-channel electronics digitizing the PMT anode signal with a step of 12.5 ns. The angular acceptance of the facility was 0.75 sr. The facility was lifted on an attached balloon in moonless and cloudless winter nights at an altitude of 300 to 900 m above the surface of the lake Baikal. It recorded EAS Cherenkov light reflected from the snow blanket of the lake. The results of these measurements were used to deduce the PCR energy spectrum and to estimate the fraction of the light cosmic-ray component. The results were reported in [14].

### 3. DEVELOPMENT AND DESIGN OF THE SPHERE-3 FACILITY

The SPHERE-3 facility, which is a new instrument for detecting reflected Cherenkov light, is being developed at the present time. It would differ from the previous version by a wider aperture, a better spatial resolution, and a high efficiency of operation. Modern silicon photomultipliers (SiPM) involving light collectors will be used as light receivers.

In order to lift the new facility above the snow surface, it is planned to employ an unmanned aircraft system—for example, the Aladdin (Al-1) vertical-takeoff aircraft having a hybrid propulsion system that can be powered from an accumulator bank and/or from a petrol engine. The bearing capacity of such an unmanned vehicle is up to 250 kg, and its size is 1 to 3 m. The flight time is expected to be 4 h. The aerodynamic scheme of the vehicle (12 engine-propeller combinations) is intended for ensuring a high bearing capacity at small dimensions and a high fault tolerance. The vehicle admits an uneventful landing even in the case of failure of up to four engine-propeller combinations and can continue the flight in the case of failure of two of them.

Below, we present some results of the development and simulation of elements of the facility and the light-detection process.

#### 3.1. Detector Structure

In the SPHERE-3 facility, use is made of a modified Schmidt optical system involving a lens corrector of spherical aberrations. Figure 1 shows a preliminary version of the structure of the frame formed by aluminum tubes 20 mm in diameter, which connects all elements of the optical system: mirror (1); lens hood (2), which cuts off side flares; lens correcting spherical aberrations (3); and mosaic of silicon photomultipliers (4). Measuring equipment is placed in the region that is shadowed by the mosaic and which has a truncated-cone shape (5). This position of the electronics makes it possible to simplify substantially the structure and to reduce the length of the cables. The removal of heat from electronics circuits is accomplished through the hole in the lower part.

The characteristics of the SPHERE-3 detector are presented in Table 1. It is planned that the SPHERE-3 detector will have the diaphragm inlet window of effective area (the area of shadowing from the photoreceiver being subtracted) not smaller than 1 m<sup>2</sup> and an optical resolution not worse than 2000 pixels. The field of view of the facility should not be smaller than  $\pm 20^\circ$ . The ultimate characteristics will be determined after the optimization of parameters of the optical system and simulation.

#### 3.2. Structure of Optical System

As a preliminary version of the detector optical structure, we consider a somewhat modified Schmidt optical scheme—an aspherical mirror combined with a correcting plate (see Fig. 2a). The mirror is close to a spherical one—the deviation from a sphere of radius 1654 mm is less than 25 mm. The outer diameter of the mirror is 2200 mm. The telescope inlet window

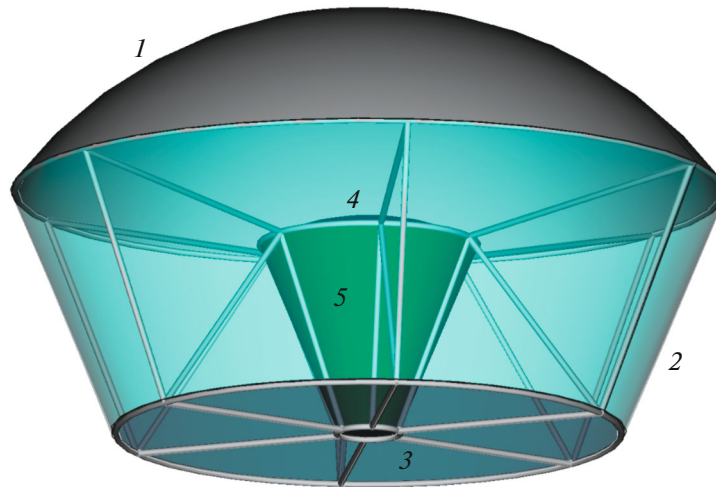


**Fig. 1.** Layout of the preliminary version of the detector: (1) mirror, (2) lens hood, (3) lens corrector, (4) SiPM mosaic, and (5) place for measuring electronics.

is closed by a correcting acrylic plate 5 to 30 mm thick and 1700 mm in diameter. This corrector has a planar outer surface and a curvilinear inner surface. This choice of orientation for the corrector was aimed at simplifying procedures for testing the invariability of geometry of the telescope upon transportation and during measurements. The light-sensitive part of the detector is formed by a SiPM mosaic of total diameter 680 mm with a sensitive area 660 mm in diameter and is placed between the mirror and corrector, along with electronics block. With allowance for shadowing by the mosaic and electronics block, the effective area of the inlet window is 1.9 m<sup>2</sup>.

Figure 2b shows the light fraction collected within a circle of specific radius in the spot. It can be seen that, for angles of up to 15°, the whole light is concentrated within a moderately small spot of radius up to 5 mm. Owing to the light collector that we describe below, the effective pixel radius is 5.6 mm. For angles approaching 20°, a wide halo of an irregular shape

appears around the spot. But even for an angle of 20°, more than 90% light is concentrated within one pixel. In Figure 2c, one can see the spots that arise upon converging parallel light beams incident to the telescope outer window at various angles (from 0° to 20°). It should be noted that the spot shapes in this panel were calculated for a spherical surface of the mosaic without taking into account the shape of the light collectors. In order to perform a complete analysis of detector operation, it is necessary to take into account the operation of the light collectors and to consider, together with them, the picture of the angular sensitivity of the detector.

### 3.3. Investigation of Lens Light Collectors

In order to improve the sensitivity of the detector, it is assumed to use light receivers. This will make it possible to reduce the number of the measurement channels and the energy consumption of the detector, on one hand, and to increase the number of photons hitting a pixel, on the other hand—that is, to lower the detection threshold. The detector structure (see Fig. 2a) assumes that light comes to the SiPM surface at sizable angles (up to 60°). The largest amount of light comes at angles in the range between 30° and 40°. In this case, the application of ordinary cone light collectors is inefficient. Lens light collectors are able to provide a large angle of light collection.

Several available lenses of various diameter and radius of curvature were studied. The test bench used and some samples subjected to study are shown in Fig. 3a. The light collector was tuned to an optical contact with SiPM and was illuminated with a source of light (LED) at a wavelength 405 nm. The angular size of the light source for the receiver was

**Table 1.** Preliminary characteristics of the SPHERE-3 detector

Parameter	Value
Sensitive area of optical system (Inlet window of diaphragm), m <sup>2</sup>	>1
Diameter of mirror, mm	up to 2200
Angle of view of optical system, deg	±25
Number of mosaic elements (silicon photomultipliers)	2000–3000
Detector mass, kg	100
Maximum altitude of lifting of detector, m	2000

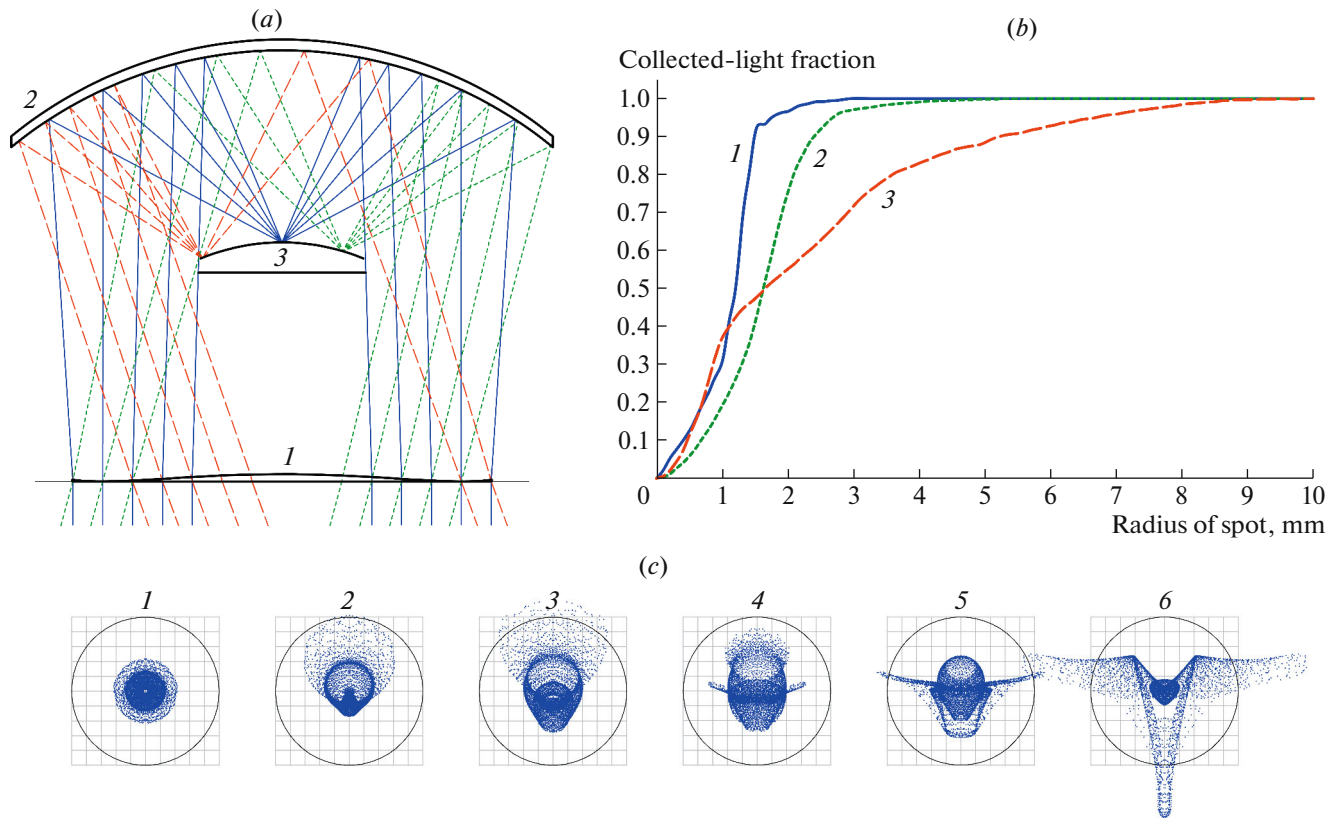


**Fig. 2.** (a) Optical scheme of the detector, which includes (1) a corrector, (2) a mirror, and (3) a SiPM mosaic, along with a picture of the propagation of rays in the case of a normal incidence to the inlet window (solid lines) and in the cases of incidence at angles of  $15^\circ$  (dashed lines) and  $20^\circ$  (dotted lines). (b) Light fraction collected within the circle of variable radius about the center of the light spot at various angles of incidence of rays to the inlet window: (1)  $0^\circ$ , (2)  $15^\circ$ , and (3)  $20^\circ$ . (c) Light-spot shape for various angles of incidence of parallel light beams to the inlet window: (1)  $0^\circ$ , (2)  $4^\circ$ , (3)  $8^\circ$ , (4)  $12^\circ$ , (5)  $16^\circ$ , and (6)  $20^\circ$ ; the grid has a step of 1 mm, and the circle shows an approximate size of a pixel 10 mm in diameter.

about  $1^\circ$ , while the step of the rocker arm with the source in the horizontal plane was  $2^\circ$ . The measurements were repeated several times upon the rotation of SiPM in the vertical plane through angles of  $10^\circ$ ,  $30^\circ$ , and  $45^\circ$ . The intensity of the constant light flux at the SiPM surface was measured on the basis of the direct current through SiPM. Figure 3b shows the results of measurements with available spherical lenses 12.5 mm in diameter having a 8-mm radius of curvature. Those measurements showed a 2.5-fold increase in the light collection for angles around  $60^\circ$  with respect to the optical axis in relation to SiPM without light collectors. In order to reach the maximum collecting power, it is planned to develop light collectors of special shape.

### 3.4. Model of SiPM Response

A model of the SensL MicroFC-60035 SiPM silicon photomultiplier intended for use in the SPHERE-3 facility is developed in order to simulate characteristics of the electronics of the measuring system in

the new detector. The response of SiPM to a single-photoelectron event is simulated.

A silicon photomultiplier can be represented in the form of a scheme that consists of a large number of Single-Photon Avalanche photodiodes (SPADs) connected in parallel. In order to simulate SiPM operation, use is made of a simplified scheme of single-photon avalanche photodiodes, which is denoted in Fig. 4 as an active cell. As an equivalent scheme of single-photon avalanche photodiodes, we consider a parallel circuit of the internal resistor of the region of the diode spatial charge and the internal capacitor of the depleted layer. The quenching scheme contains a quenching resistor  $R3$  and a capacitor  $C1$  mimicking parasitic capacitances. In order to mimic the arrival of photon, use is made of an interruptor and a power supply unit in the branch involving the resistor  $R2$  [20]. A signal whose duration corresponds to the avalanche-process time is fed from a pulsed-current source  $V2$  to the terminals of an electric interruptor  $S1$ . The closing of the interruptor leads to the discharge of the capacitor  $C1$ . This provokes

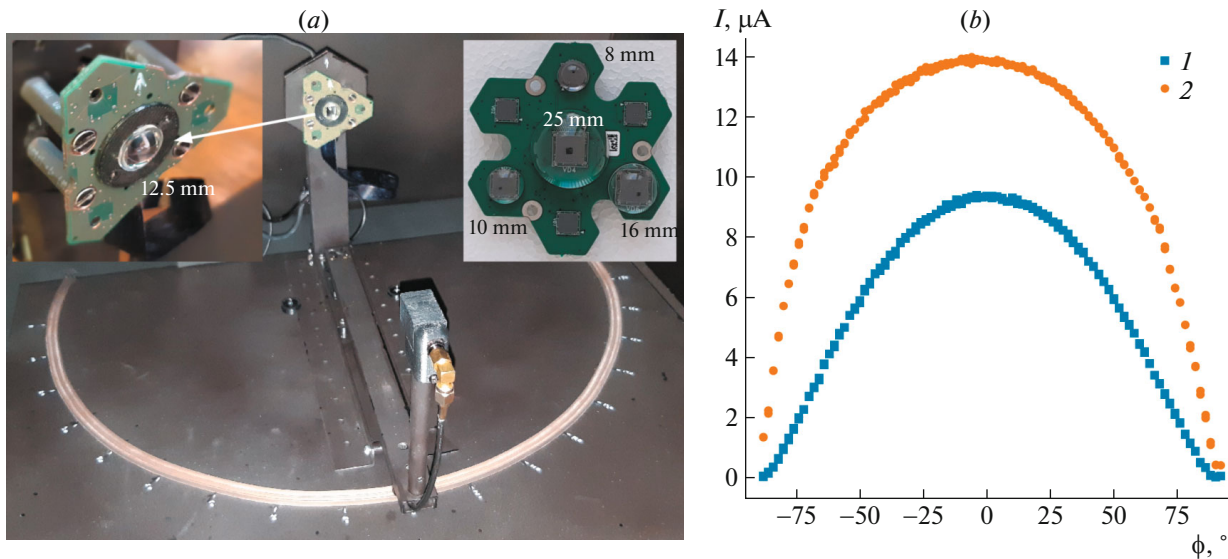


**Fig. 3.** Investigation of lens light collectors. (a) Test bench for automated measurement of the angular characteristics of the sensitivity of SiPM and light collectors. Lenses of various shape and size are tuned to an optical contact with SiPM. (b) Results obtained by measuring the sensitivity of SiPM versus the angle of light incidence to its surface for (1) SiPM without a light collector and (2) SiPM with a light collector 12.5 mm in diameter having a 8-mm radius of curvature.

an exponential drop of voltage between  $C2$  and  $C1$ . The maximum voltage drop there is governed by an internal power supply unit  $V3$  and is dependent on the temperature of SiPM operation.

The MicroFC-60035 silicon photomultiplier contains 18980 cells. In our analysis, it is assumed that the cells are able to absorb photons irrespective of each other. This makes it possible to partition the cells into two classes in order to simplify the simulation: (i) active cells—those in which photon absorption occurred (the interruptor is closed); (ii) passive cells—those in which no photon absorption event occurred (the interruptor is open).

This scheme admits the rescaling of the number of active elements and is adaptable to a simulation of other SiPM series involving a different number of cells.

The nominal parameters of the elements involved are chosen in such a way that the signal at the fast SiPM output corresponds to the experimental curve from the specifications of the manufacturer [21]. The nominal values estimated for the components are given in Table 2.

The solid line in the graph in Fig. 5 corresponds to the calculated response of the model at the fast SiPM output, while the points on display represent digitized experimental data of the SiPM manufacturer. In order to match the resulting pulse-shape curve at the SiPM output with the data of the manufacturer, the model was supplemented with the fast-output capacitor  $Cx$  that takes into account the parasitic capacitance of the cable connecting the detector to an oscilloscope.

Having a silicon-photomultiplier model at our disposal, we can determine the characteristics of measuring equipment.

### 3.5. Measuring Equipment

A segment of several SiPMs is a basic element of the Cherenkov light detector in the new facility. A similar segment formed by seven SiPM was developed by our group earlier [22] and is shown in Fig. 3a. Tests of the matrix formed by seven such segments, which contains in all 49 SiPMs, was completed in 2018; since September 2019, this matrix has been successfully exploited in the composition of the SIT telescope used at the TAIGA complex array [23, 24]. In the new detector, it is planned to elaborate on the SiPM segment and to adapt it for use in an optical system featuring lens light collectors.

**Table 2.** Nominal parameters of the components used in the scheme in Fig. 4

	Nominal		Nominal		Nominal
$R1$	0.01 $\Omega$	$C1$	0.18 pF	$V1$	27 V
$R2$	392 k $\Omega$	$C2$	0.55 fF	$V2$	Generator 1.75 ns
$R3$	4.15 k $\Omega$	$C3$	2.52 fF	$V3$	24.5 V
$R4$	0.01 $\Omega$	$C4$	48 pF		
$R5$	20.63 $\Omega$	$C5$	3400 pF		
$R6$	50 $\Omega$	$C6$	10.45 pF		

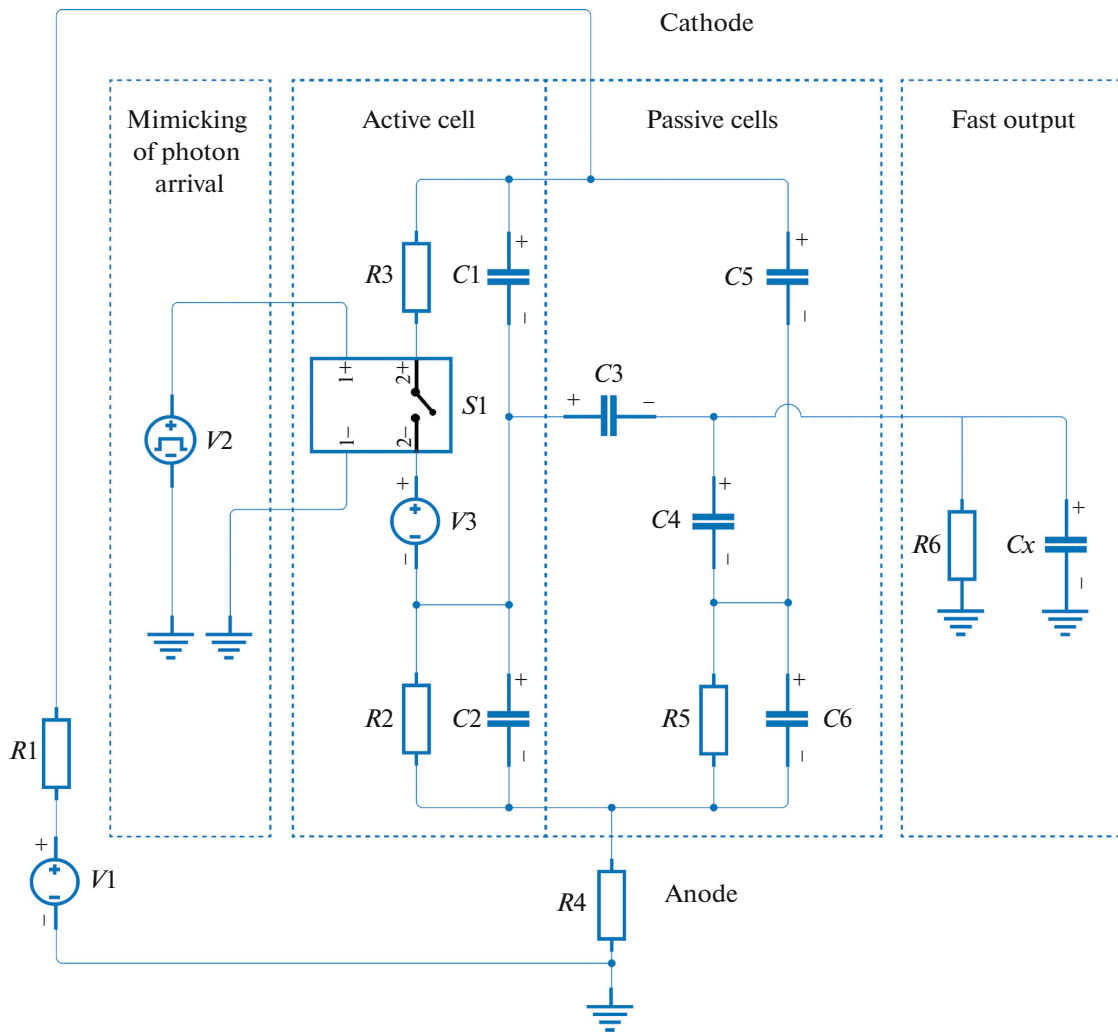
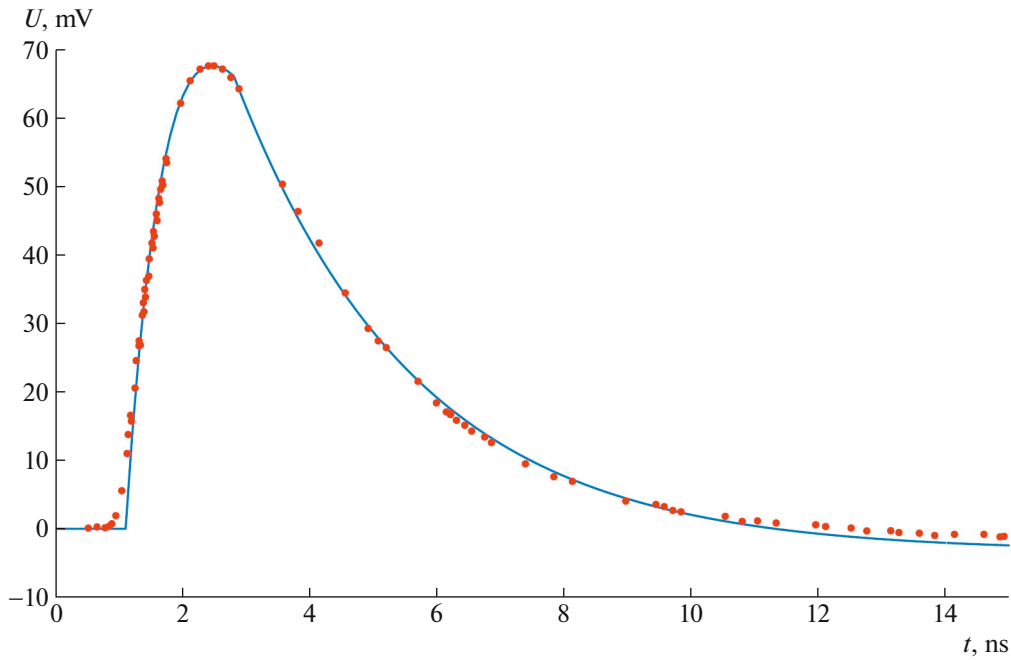


Fig. 4. Layout of the SiPM structure model.

A circuit board on the basis of the microcircuit of an eight-channel fast analog-to-digital converter (ADC) is developed for recording amplified analog signals from SiPMs. A digitizing frequency of 80 to 100 MHz and an amplitude resolution of 12 to 14 bits provide a dynamical range of up to  $10^4$ . Owing to small dimensions of the ADC microcircuit ( $9 \times 9$  mm), the measuring circuit can be arranged near the circuits of the SiPM segments immediately under the mosaic (see Fig. 1). This configuration makes it possible to reduce substantially the mass and dimensions of the detector. Digitized signals from each channel are transferred in a sequential code through the LVDS interface to the microcircuit of programmed logic. The whole intrinsic logic of operation of the measuring system and a local trigger for event selection is downloaded to the microcircuit in the form of a configuration file. The results of measurements are saved on a microSD card of the

embedded computer of each measuring circuit for subsequent clustering and processing.

The signals are digitized continuously, but, technically, it is next to impossible to conserve a data flow of up to 500 Gb/s; moreover, this is not necessary in practice. A triggering circuit is developed in order to single out useful events in the data flow. This circuit receives signals from digital amplitude discriminators in each measuring channel. In response to the actuation of the discriminators in three or more neighboring channels within  $1 \mu\text{s}$ , the circuit transfers a confirmation signal to all measuring circuits, which, in turn, move data within the interval of 10 to  $20 \mu\text{s}$  prior to and after the arrival of the trigger confirmation signal from RAM to a permanent storage. The volume of one such event, together with calibration data, will be about 25 Mb. It is expected that the maximum trigger-actuation frequency will not exceed 1 Hz. A mathematical model for choosing an optimum algorithm of operation of the system that would separate



**Fig. 5.** Pulse at the SiPM output: Voltage  $U$  at the fast output as a function of time  $t$ . The solid curve represents the response of the model, while the points on display stand for experimental data of the manufacturer [22].

useful signals from the background (generation of a trigger signal) is developed on the basis of the accumulated sample of model events.

#### 4. SIMULATION

##### 4.1. Approximation of the Lateral Distribution of EAS Cherenkov Light

The objectives pursued by the SPHERE experiments include estimating the primary-particle mass. The mass-estimation criterion used in the SPHERE experiments [25] is based on the measured shape of the lateral distribution of the EAS Cherenkov light and is defined as the ratio of the integrals of the total number of Cherenkov photons over rings that have different radii. In employing this criterion for the primary-particle mass, the region in the vicinity of the shower axis carries important information about the primary-particle mass; therefore, the function used should well approximate the features of EAS in the region between 0 to 300 m.

In order to simulate a SPHERE type facility, the distribution  $I(R)$  of the EAS Cherenkov light at the Earth’s surface is approximated in the form

$$F = \frac{p_0}{(1 + p_1 R + p_2 R^2 + p_3 R^3)} w_1 + \frac{p_4}{(1 + p_5 R + p_6 R^2)} w_2, \quad (1)$$

$$w_1 = \frac{1}{(1 + \exp((R - R_{ch})/s))}, \quad (2)$$

$$w_2 = \frac{1}{(1 + \exp(-(R - R_{ch})/s))},$$

where  $R$  is the distance from the shower axis and  $p_1, \dots, p_6$ , and  $R_{ch}$  are adjustable parameters.

The function  $F$  approximating the lateral distribution of EAS Cherenkov light (see Fig. 6a) deviates from the model distribution  $I(R)$  by less than 10% in the range of distances between 0 and 500 m from the shower axis (see Fig. 6b); in the region between 0 and 100 m, the relative error  $d = (I(R) - F(p_1, \dots, p_6, R_{ch}, R))/I(R)$  does not exceed 2% in the majority of cases and grows with increasing distance from the axis. This accuracy of the function approximating the lateral distribution of EAS Cherenkov light is appropriate for use of the primary-mass criterion. For the details of the simulation performed in searches for this approximation, the interested reader is referred to [26]. Originally, the approximation in (1) was intended for processing events of the SPHERE-2 experiment, but it can be applied to any experiment that employs the lateral distribution of EAS Cherenkov light at the Earth’s surface level.

##### 4.2. Inclusion of Mirror Distortions

The spherical mirror creates, on the detector mosaic, an image whose shape is distorted in relation to the shape of the object under study. An analysis of Cherenkov EAS images in the field of view of the telescope of the SPHERE type with the aim of estimating the primary-particle mass requires taking into

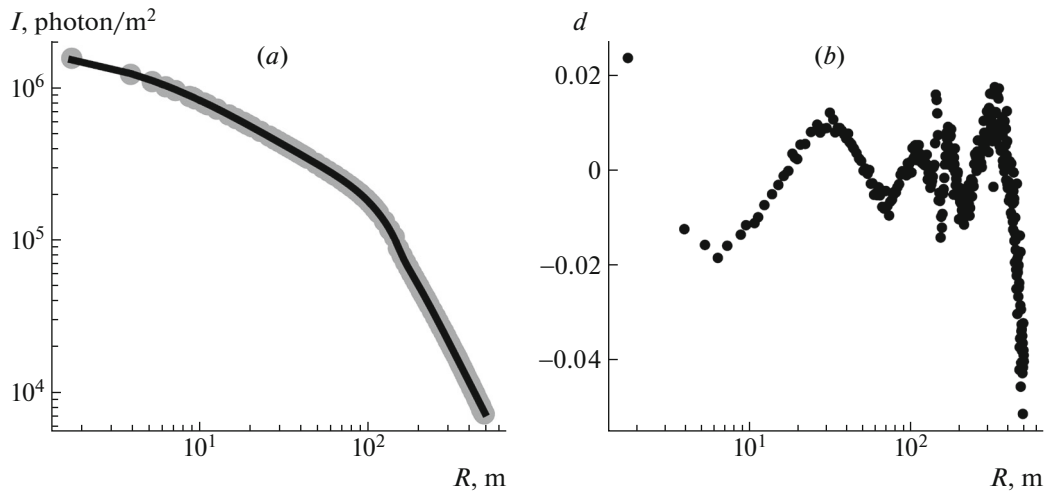


**Fig. 6.** (a) Azimuthal-angle-averaged lateral distribution of EAS Cherenkov light for an individual EAS event. Simulated points of  $I(R)$  are marked in gray, and the curve represents the approximating function  $F$  in the form (1). (b) Relative deviation of the approximating curve  $F$  from simulated points.

account these distortions since, in data processing, the images are approximated by an axially symmetric function. An algorithm for calculating functions that would correct distortions of a spherical mirror is constructed.

The calculation was performed for the following simplified configuration of the optical system: a spherical mirror of radius 1100 mm (its radius of curvature is 1400 mm), a mosaic in the form of a spherical segment with a radius of 340 mm (its radius of curvature is 750 mm), and the inlet diaphragm of radius 660 mm. The centers of curvature of the mirror and mosaic coincide, and the diaphragm plane is 100 mm apart from this point along the axis of the system in the direction opposite to that toward the mosaic. The detector scans the snow surface under itself from the altitude of 1000 m.

A sequence of pointlike objects on the snow that go away from the telescope axis with a constant step and the sequence of the centers of gravity of the clouds of their images on the mosaic were viewed. We denote by  $r$  the distance from the telescope axis to the points on the snow and by  $\rho$  the distance from the center of the mosaic to the images of these points.

In Figure 7a, the distance  $\rho$  from the center of the mosaic to the image as a function of the distance  $r$  from the telescope axis to the respective point on the snow is shown by the dashed line according to the results of the simulation of ray propagation in the optical system. This dependence is nonlinear. Specifically, the projections of the distance on the snow,  $r$ , onto the mosaic are compressed toward the edge of the mosaic. There are no distortions on the axis ( $r = 0$ ), and we can draw a linear dependence (solid line in Fig. 7a) representing a corrected distance  $\rho'$

from the axis to the image as a tangent to the curve at the point  $r = 0$ .

It is noteworthy that spherical distortions also lead to a change in the amount light collected by photosensors that are formally of the same area, but which are situated at different distances from the center of the mosaic. A photosensor-area element written in the system of polar coordinates  $(\rho, \varphi)$  has the form  $dS = \rho d\rho d\varphi$ , where  $\rho$  is the distance to area element on the mosaic. Since the distortion depends only on the radius, the area element in the corrected coordinate system has the form  $dS' = \rho' d\rho' d\varphi$ . Figure 7b shows the function that relates the corrected linearized distance  $\rho'$  to the original distorted distance  $\rho$  on the mosaic and which was calculated on the basis of the ratio of the curve and straight line in Fig. 7a. The corrected distance  $\rho'$  exceeds the original distance  $\rho$ ; therefore, the area element after correction,  $dS'$ , is larger; that is, the distortions of the spherical mirror lead to a compression of the light flux. Thus, a photosensor whose center is at a distance  $\rho$  from the axis has the effective area larger by the factor

$$\zeta(\rho) = \frac{dS'}{dS} = \frac{\rho' d\rho'}{\rho d\rho}. \quad (3)$$

In order to correct the image, the number of photons in it should be reduced by the factor  $\zeta(\rho)$ . The function  $\zeta(\rho)$  is shown in Fig. 8a.

If the snow surface is illuminated uniformly, the brightness of the mosaic increases toward the edges. This increase is determined by the geometry of the optical scheme and should be taken into account as yet another distortion of a spherical mirror. The ultimate dependence of the relative brightness  $\delta(\rho)$

normalized to its maximum value is shown in Fig. 8*b*. The details of the calculation can be found in [27].

#### 4.3. Separation of Primary Particles in Mass for Nearly Vertical Showers

The ability to see the spot of Cherenkov light from EAS on the snow surface with a spatial resolution of 30 to 80 m depending on the altitude of observation is an important feature of the SPHERE-2 telescope. The scanned part of the total area of the spot of EAS Cherenkov light is about 30%. The ability to observe the spot region lying around the shower axis and having a radius of about 150 m is of paramount importance since this region carries valuable information about the primary-particle mass. The projected telescope SPHERE-3 is assumed to feature a substantially greater number of pixels in the mosaic, and they will be distributed more densely. This would improve the spatial resolution of the telescope and increase the fraction of the observed spot area. The telescope design and the algorithm for processing images are assumed to be optimized with an eye to tackling the problem of event separation in primary mass.

The first parameters that could be used as criteria sensitive to the primary mass and which are based on direct measurements were found before the commissioning of the SPHERE-2 telescope [25]. These parameters made use of the characteristic behavior of the lateral distribution of EAS Cherenkov light: on average, the steepness of this distribution in the near-axis region decreases with increasing mass of the primary nucleus at the same primary energy. The main problem of shower separation in primary mass is due to the presence of cascade fluctuations leading to significant deviations of the steepness from average values.

A good criterion should permit estimating primary mass with a minimum error for given experimental conditions (detector design, geometry of measurements, background level, etc.). For this, it should satisfy the following requirements. First, it should be based on directly measurable features of EAS or on features calculable from the results of direct measurements with the aid of a minimal set of approximations. Second, it should be expressed in terms of integrals of measurable features, since the impact of signal and background fluctuations is suppressed partly in this case. Third, it should rely on signatures of the shape of measured distributions. The last property makes it possible to alleviate substantially the dependence of the resulting criterion on the nuclear-interaction model, which introduces a significant uncertainty in the estimation of the primary mass.

The results of the SPHERE-2 experiments were analyzed in terms of a criterion in the form of the ratio of the integrals of an axially symmetric approximation of the lateral distribution of EAS Cherenkov light on the snow surface over two regions: over the circle whose center lies on the axis and whose radius is 70 mm and over the ring surrounding this circle and having an external radius of 140 m [25]. This criterion permitted partitioning all nuclei into a light and a heavy component. For this, the lateral distribution of the image on the mosaic had to be rescaled to the lateral distribution on the snow surface. At the present time, work on developing criteria based on the shape of the distribution directly on the mosaic is under way. New parameters as criteria for targeted ranges of primary parameters are being constructed for SPHERE-2, as well as for ranges planned for study with SPHERE-3. Since estimation of the primary mass is chosen for the priority task of the new experiment, a comparison of the results obtained by classifying events in primary mass for various versions of the detector design would make it possible to optimize this design.

For basic nuclei ( $^1\text{H}$ ,  $^{14}\text{N}$ , and  $^{56}\text{Fe}$ ), the errors of the classification for the SPHERE-2 detector are about 0.30 (see Fig. 9); moreover, the choice of criteria for which these errors were virtually independent of the nuclear-interaction model (this was so for the QGSJET01 and QGSJETII-04 models) turned out to be possible. The data obtained by means of the SPHERE-2 telescope will be revisited on the basis of new criteria. In doing this, a consistent individual approach will be applied: estimations of all primary parameters will be performed for each event. After that, the partition into groups in mass will admit different implementations depending on the pursued objective. All elaborations upon the methods for processing SPHERE-2 data will be extended to the respective methods for the SPHERE-3 detector.

Elaboration on the SPHERE-3 design and its optimization will make it possible to improve the resolution in primary mass via taking into account a number of factors in data processing. The processing methods will be developed along two lines. The first will involve taking into account distortions introduced by the mirror and corrector and constructing a more adequate approximation of the image on the mosaic of the telescope. The second is the search for optimum criteria on the basis of the best approximation of the image shape that are the most sensitive to the primary mass. In particular, use will be made of multidimensional criteria based on at least two features of the image shape. In that case, the separation of events into preset groups of nuclei is not a pursued objective. The classification process is needed only for choosing the most sensitive criteria.

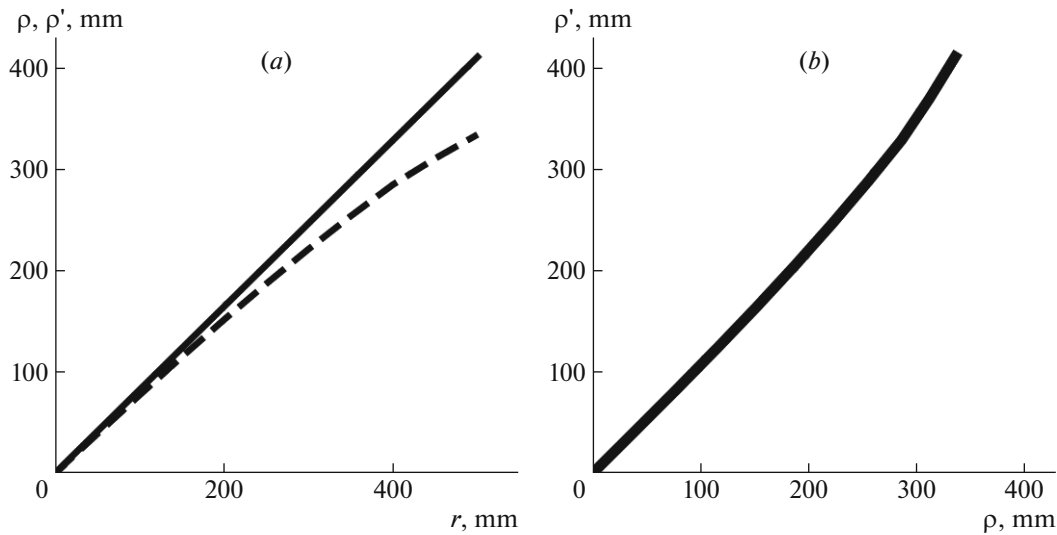


**Fig. 7.** (a) Distorted distance  $\rho$  (dashed curve) and corrected distance  $\rho'$  (solid curve) from the center of the mosaic to the image versus the distance  $r$  from the telescope axis to the point on the snow. (b) Function relating the distorted distance  $\rho$  to the corrected distance  $\rho'$  on the mosaic.

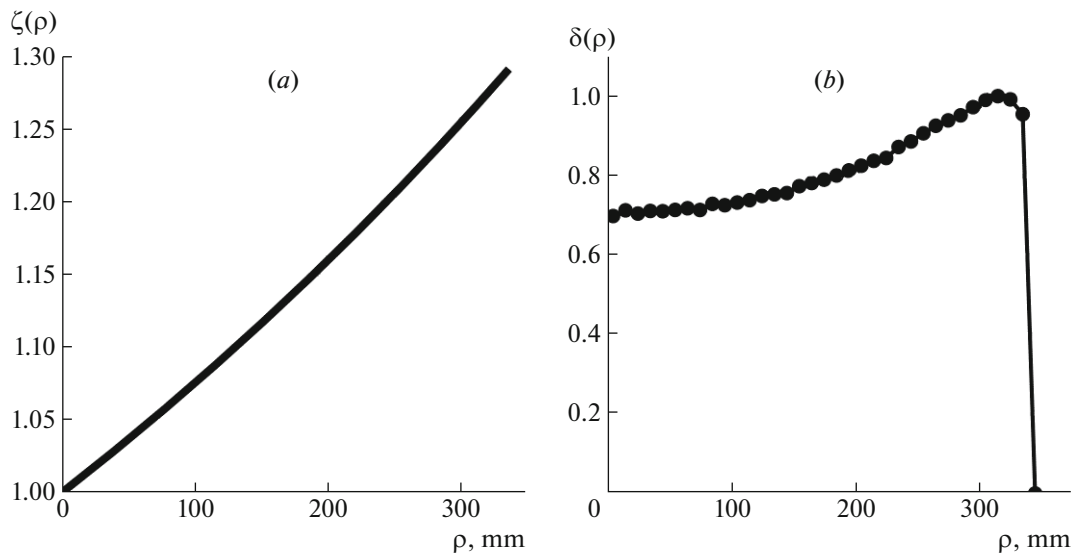


**Fig. 8.** (a) Coefficient  $\zeta(\rho)$  of the decrease in the number of photons in the photosensor as a function of the distance  $\rho$  on the mosaic; (b) relative brightness of the image,  $\delta(\rho)$ , as a function of the distance  $\rho$  from the center of the mosaic.

## 5. SEARCH FOR NEW METHODS AIMED AT IMPROVING THE SEPARATION OF PCR COMPONENTS

The Schmidt optical system with a lens correcting spherical aberration will be used in the SPHERE-3 detector. In this system, the central part of the mirror is not involved, since it is in the shadow of the photoreceiver. This region may be used to record direct Cherenkov light through the holes in the mirror. Calculations show that, for EAS from 10-PeV PCR, the flux of Cherenkov light is about 150 photons per  $1 \text{ cm}^2$  at a distance of 100 m from the shower axis.

With allowance for the SiPM photon detection efficiency (PDE), which is about 40%, and at losses of up to 75% on optical elements, it is possible to record about 45 photoelectrons from  $1 \text{ cm}^2$ . Signals from direct and reflected Cherenkov light are detected individually, since the times of their arrival to the detector differ by  $3.3 \mu\text{s}$  at the detector altitude of 500 m. In estimating the composition of PCR, information about the intensity of direct Cherenkov light can be used as complement to data on reflected Cherenkov light. The light spot formed on the photoreceiver by EAS from a primary proton is expected to have an angular size

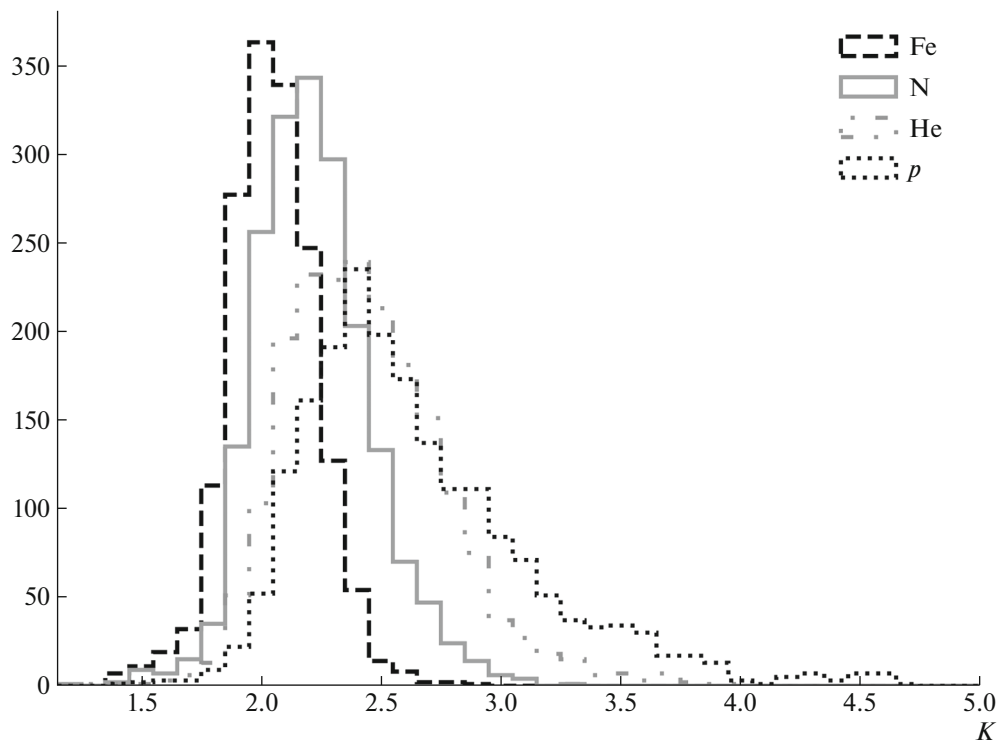


**Fig. 9.** Histograms of the distributions of the parameters  $K$  used as criteria for  $E = 10$  PeV, an inclination angle of  $15^\circ$ , atmosphere model 11 from the CORSIKA list, and the observation altitude of 900 m for the SPHERE-2 detector. The Cherenkov images of EAS were approximated by an axially symmetric function, and the ratio of the integrals of this function over optimum regions was taken to be the parameter used as a criterion.

larger than that of the spot associated with primary iron nuclei at the same primary energy and the same depth of the maximum of development of the cascade of secondary particles [28]. It is planned to perform an investigation aimed at assessing the efficiency and advisability of detection of direct Cherenkov light in order to reach the goal of the project.

The spectrum of EAS Cherenkov light has a broad distribution extending from a deep ultraviolet region to an infrared region. However, its intensity is insignificant in the infrared region. As for the ultraviolet component, it is absorbed by the Earth's atmosphere. Nevertheless, an ultraviolet part (characterized by wavelengths shorter than 350 nm) of EAS Cherenkov light is present in the light flux arriving at the Earth's surface. This light is generated by the damped EAS cascade in the lower atmosphere, where the ozone concentration is insignificant. At PCR energies in excess of 1 PeV, such extended cascades may be generated by protons and light nuclei. Of course, this Cherenkov light in the ultraviolet range forms a small fraction in the total flux, but its specific fraction in the near-axis region of EAS may be sufficient to be recorded by the developed detector. As a rule, modern detectors of Cherenkov light record most efficiently the region between 400 and 500 nm, where photomultiplier tubes and SiPM have the highest sensitiv-

ity. In order to separate the ultraviolet component of Cherenkov light, it is planned to use two SiPM types in the photoreceiver—specifically to supplement ordinary SiPMs, which are sensitive to wavelengths longer than 300, with SiPMs whose sensitivity is enhanced in the range between 250 and 300 nm. An arrangement of these two types in a staggered order would permit discriminating between the components of the flux of EAS Cherenkov light. The hypothesis that the light component of PCR can be separated at the instrumental level will be tested on the basis of a mathematical simulation.

## 6. CONCLUSIONS

General principles of the design of the optical system for the SPHERE-3 detector have been developed. Searches for optimum parameters of the detector optical elements, including a mirror, a correcting lens, a photoreceiver with SiPMs, and lens light collectors, are being performed. The characteristics of samples of available lens light collectors have been studied. The response of SiPM to a single-photoelectron event has been simulated. A simulation aimed at searches for criteria of separation of events induced by primary cosmic rays of different type and

at the improvement of these criteria has been continued. Searches for a SPHERE-3 carrier are being performed.

The SPHERE-3 detector, which detects reflected EAS Cherenkov light, will make it possible to obtain new information about the chemical composition of PCR in the energy range between 1 and 1000 PeV. In particular, it is planned to obtain experimental data for determining partial spectra for several groups of PCR (protons, CNO groups, and Fe) in this energy range on the basis of processing individual EAS events. Data on the composition of PCR in the energy range being considered would be of decisive importance for the choice of model for the transition from galactic cosmic rays to extragalactic ones. This in turn is of importance for constructing a global picture of the acceleration and propagation of cosmic rays in the Universe.

## REFERENCES

1. S. Thoudam, J. P. Rachen, A. van Vliet, A. Achterberg, S. Buitink, H. Falcke, and J. R. Hörandel, *Astron. Astrophys.* **595**, A33 (2016).
2. F. G. Schöder, *PoS (ICRC2019) 030* (2019).
3. Pierre Auger Collab., *Phys. Lett. B* **762**, 288 (2016).
4. A. Glushko and A. Sabourov, *JETP Lett.* **98**, 655 (2013).
5. W. D. Apel, J. C. Arteaga-Velázquez, K. Bekk, M. Bertainia, J. Blümer, H. Bozdog, I. M. Brancus, E. Cantoni, A. Chiavassa, F. Cossavella, K. Daumiller, V. de Souza, F. di Pierro, P. Doll, R. Engel, J. Engler, et al., *Astropart. Phys.* **47**, 54 (2013).
6. T. Antoni, W. D. Apel, A. F. Badea, K. Bekk, A. Bercuci, J. Bümer, H. Bozdog, I. M. Brancus, A. Chilingarian, K. Daumiller, P. Doll, R. Engel, J. Engler, F. Fßler, H. J. Gils, R. Glassttter, et al., *Astropart. Phys.* **24**, 1 (2005).
7. M. G. Aartsen et al., *Phys. Rev. D* **88**, 042004 (2013).
8. The IceCube Collab., *PoS (ICRC2019) 014* (2019).
9. H. P. Dembinski, R. Engel, A. Fedynitch, T. Gaisser, F. Riehn, and T. Stanev, *PoS (ICRC2017) 533* (2017).
10. A. E. Chudakov, in *Experimental Methods for Studying Ultrahigh-Energy Cosmic Rays: Proceedings of the All-Union Symposium, Yakutsk, June 19–23, 1972* (Yakutsk. Fil. Sib. Otd. Akad. Nauk SSSR, 1974), p. 69.
11. T. C. Weekes, M. F. Cawley, D. J. Fegan, K. G. Gibbs, A. M. Hillas, P. W. Kowk, R. C. Lamb, D. A. Lewis, D. Macomb, N. A. Porter, P. T. Reynolds, and G. Vacanti, *Astrophys. J.* **342**, 379 (1989).
12. A. V. Plyasheshnikov, A. K. Konopelko, F. A. Aharonian, M. Hemberger, W. Hofmann, and H. J. Völck, *J. Phys. G* **24**, 653 (1998).
13. R. A. Antonov, T. V. Aulova, E. A. Bonvech, D. V. Chernov, T. A. Dzhatdoev, Mich. Finger, Mir. Finger, V. I. Galkin, D. A. Podgrudkov, and T. M. Roganova, *J. Phys.: Conf. Ser.* **632**, 012090 (2015).
14. R. A. Antonov, T. V. Aulova, E. A. Bonvech, V. I. Galkin, T. A. Dzhatdoev, D. A. Podgrudkov, T. M. Roganova, and D. V. Chernov, *Phys. Part. Nucl.* **46**, 60 (2015).
15. R. A. Antonov, E. A. Bonvech, D. V. Chernov, T. A. Dzhatdoev, M. Finger, Jr., M. Finger, D. A. Podgrudkov, T. M. Roganova, A. V. Shirokov, and I. A. Vaiman, *Astropart. Phys.* **121**, 102460 (2020).
16. R. A. Antonov, E. A. Bonvech, D. V. Chernov, D. A. Podgrudkov, and T. M. Roganova, *Astropart. Phys.* **77**, 55 (2016).
17. E. A. Bonvech, D. V. Chernov, M. Finger, M. Finger, V. Galkin, D. Podgrudkov, T. Roganova, and I. Vaiman, *Universe* **8**, 46 (2022).
18. R. A. Antonov, S. P. Beschapov, E. A. Bonvech, D. V. Chernov, T. A. Dzhatdoev, Mir. Finger, Mix. Finger, V. I. Galkin, N. V. Kabanova, A. S. Petkun, D. A. Podgrudkov, T. M. Roganova, S. B. Shaulov, and T. I. Sysoeva, *J. Phys.: Conf. Ser.* **409**, 012088 (2013).
19. R. A. Antonov, T. V. Aulova, S. P. Beschapov, E. A. Bonvech, D. V. Chernov, T. A. Dzhatdoev, Mir. Finger, Mix. Finger, V. I. Galkin, N. V. Kabanova, A. S. Petkun, D. A. Podgrudkov, T. M. Roganova, S. B. Shaulov, and T. I. Sysoeva, in *Proceedings of the 33rd International Cosmic Ray Conference, Rio de Janeiro, 2014*, p. 1185.
20. S. Gundacker and A. Heering, *Phys. Med. Biol.* **65**, 17 (2020).
21. Silicon Photomultipliers (SiPM), Low-Noise, Blue-Sensitive C-Series SiPM Sensors, Rev. 1.0 (SensL Inc., 2014).
22. D. Chernov, E. Bonvech, T. Dzhatdoev, Mir. Finger, Mich. Finger, V. Galkin, G. Garipov, V. Kozhin, D. Podgrudkov, and A. Skurikhin, *J. Phys.: Conf. Ser.* **1181**, 012025 (2019).
23. D. Chernov, I. Astapov, P. Bezyazeekov, E. Bonvech, A. Borodin, M. Brueckner, N. Budnev, D. Chernukh, A. Chiavassa, A. Dyachok, O. Fedorov, A. Gafarov, A. Garmash, V. Grebenyuk, O. Gress, T. Gress, et al., *J. Instrum.* **15**, C09062 (2020).
24. D. A. Podgrudkov, E. A. Bonvech, I. A. Vaiman, D. V. Chernov, I. I. Astapov, P. A. Bez'yazykov, M. Blank, A. N. Borodin, M. Bryukner, N. M. Budnev, A. V. Bulan, A. Vaidyanatan, R. Vishnevskii, P. A. Volchugov, D. M. Voronin, A. R. Gafarov, et al., *Bull. Russ. Acad. Sci.: Phys.* **85**, 408 (2021).
25. V. I. Galkin and T. A. Dzhatdoev, *Bull. Russ. Acad. Sci.: Phys.* **75**, 309 (2011).
26. V. S. Latypova and V. I. Galkin, *Uch. Zap. Fiz. Fak-ta Mosk. Univ.* (2022, in press).
27. K. Zh. Azra and V. I. Galkin, *Uch. Zap. Fiz. Fak-ta Mosk. Univ.* (2022, in press).
28. R. Bakhromzod and V. I. Galkin, *Nucl. Instrum. Methods Phys. Res., Sect. A* **1018**, 165842 (2021).